Originally published as:

In-situ CHAMP observation of ionosphere-thermosphere coupling

Hermann Lühr[1], Jaeheung Park[1,2], Patricia Ritter[1], and Huixin Liu[3]

1) Deutsches GeoForschungsZentrum, GFZ, Telegrafenberg, 14473 Potsdam, Germany
2) Department of Physics, Korea Advanced Institute of Science and Technology (KAIST), Daejeon, Republic of Korea.
3) Research Institute for Sustainable Humanosphere, Kyoto University, Uji, Japan.

Abstract. The coupling between the ionised plasma and the neutral thermospheric particles plays an important role for the dynamics of the upper atmosphere. Significant progress in understanding the related processes has been achieved thanks to the availability of continuous accurate measurements of thermospheric parameters like mass density and wind by high resolution accelerometers on board the satellites CHAMP and GRACE. Here we present some examples of ionosphere-thermosphere coupling where CHAMP observations contributed considerably to their interpretation. We start with the derived properties of the thermosphere at altitudes around 400 km. A new aspect is the significant control of the geomagnetic field geometry on thermospheric features. Phenomena discussed in some depths are the equatorial mass density anomaly, the cusp-related mass density enhancement and the thermospheric response to magnetospheric substorms. Here we consider both the effect on the density and on the wind. A long predicted process is the wind-driven ionospheric F region dynamo. The high-resolution magnetic field measurements of CHAMP enabled for the first time a systematic study of that phenomenon considering longitudinal, local time, seasonal and solar flux dependences. Some open issues that require further investigations are mentioned at the end.

1. Introduction

The Earth's atmosphere up to about 100 km altitude can be considered as well mixed. The relative abundance of the main constituents stays about the same as near the surface. Above 100 km the mean free path between collisions becomes increasingly larger. Therefore the constituents start to separate and decay with increasing height following their individual barometric law. The height range 100-1000 km is commonly termed thermosphere. Here the extreme ultraviolet (EUV) radiation of the sun (5~100 nm wavelength) is almost completely absorbed. This causes the temperature to rise with increasing altitude from its minimum of about 180 K to above 1000 K. The solar EUV radiation causes also a dissociation of the gas molecules. In particular, atomic oxygen is created from O_2. Because of its lighter weight and fairly large number density, atomic oxygen is the most abundant species in the height range 200 ~ 1000 km. A general introduction into the properties of the thermosphere is given, for example, by Prölss (2004).
Another effect of the high energetic solar radiation is the partial ionisation of atoms and molecules. The ionised component of the upper atmosphere is called ionosphere, and it is immerged in the thermosphere. The vertical structure of the electron density is determined by the balance between ionisation rate and recombination rate. Largest electron densities are typically found in the F region at altitudes between 250 - 300 km. Another layer forms during daytime around 115 km altitude. This so-called E region disappears during night due to the high recombination rate and the

lack of solar insulation. In the F region the recombination rate is much lower. Therefore it persists throughout the night.

The thermosphere and the ionosphere particles show different dynamic behaviour. The neutrals are driven by hydrodynamic forces, but the ions are controlled in addition by electrodynamic forces. Due to frequent collisions between ions and neutrals the frictional force enters the momentum equations of both species as a further term. The coupling between the ionospheric plasma and the neutral thermosphere is particularly strong in the E-layer between 100 and 120 km altitude during day time. Here the horizontal conductivity peaks, and any electric field mapped into this layer will drive currents. Since the electrical conductivity along magnetic field lines is very high, the ionospheric E and F regions are electromagnetically coupled. During day time the highly conductive E region shorts out most of the F region voltages while at night the E region behaves as an open circuit. More details about the ionospheric electrodynamics can be found, for example, in Kelley (2009).

The mass density of the thermosphere is several orders of magnitude larger than that of the ionospheric plasma. Therefore, any heat generated by the dissipation of ionospheric currents is dumped into the thermosphere, and the thermospheric temperature determines largely the ion temperature, at least up to ~400 km altitude.

In the subsequent sections we will present primarily CHAMP observations of coupling processes between ions and neutrals taking place at altitudes around 400 km. At this height range the thermosphere is largely dominated by atomic oxygen, and, in terms of the ionosphere, being generally above the F region density peak, the most abundant ion is single charged oxygen (O^+). The coupling between ions and neutrals can be considered weak at that altitude. Nevertheless, several important coupling processes are taking place there. In this article we will report about the most prominent ones.

2. CHAMP satellite measurements

The data presented here are primarily measured by the German satellite CHAMP (**CHA**llenging **M**inisatellite **P**ayload). CHAMP was launched into a circular, near-polar (inclination: 87.2°) orbit at 456 km altitude (Reigber et al., 2002). Over its 10 years life time the orbit slowly decayed, and reentry into the atmosphere occurred on 19 September 2010. Due to the chosen inclination, the orbital plane precessed through local time at a rate of 1 hour per 11 day. It thus took CHAMP 131 days to sample all local times on ascending and descending orbital arcs. When considering a time period of 5 years the local time distribution of CHAMP readings is evenly distributed over all seasons. For that reason a 5-year interval is most suitable for a statistical study.

A schematic picture of the CHAMP satellite is shown in Figure 1. The spacecraft is 3-axes stabilised, pointing with the boom into flight direction. The scientific payload consists among others of a scalar magnetometer at the boom tip. This absolute instrument is used for magnetic calibration purposes. A fluxgate magnetometer is mounted at the centre of the boom, together with a pair of star cameras for precise altitude determination. Readings of the vector magnetometer are employed for the determination of ionospheric currents. A planar Langmuir probe (PLP) faces into the ram direction. From its readings the electron density and the electron temperature can be deduced. Of particular interest for the results presented here is the accelerometer accommodated at the satellite's center of gravity. At this position it senses only the non-gravitational forces acting on the spacecraft. The measurement principle is based on a proof-mass of about 100g that is kept floating in the center of a vacuum cage by electrostatic forces. The acceleration acting on the spacecraft body is deduced from the restoring forces in the three spatial directions that are required to keep the proof-mass in the center.

From the air drag experienced by the satellite the thermospheric mass density and wind can be deduced.

102   The basis equation is

$$\boldsymbol{a} = -\frac{1}{2}\rho\frac{\boldsymbol{C_d}}{m}A_{eff}\,v^2 \qquad\qquad (1)$$

104   where $\boldsymbol{a}$ is the measured acceleration, ρ is the mass density, m is the satellite mass, A_{eff} denotes the
105   effective cross-section area in ram direction and v the velocity of the satellite. $\boldsymbol{C_d}$ is the drag
106   coefficient vector with different values for along-track and cross-track directions.
107   Equ. (1) can be solved for the mass density, ρ, since the other quantities are known or measured.
108   Further details about the interpretation of accelerometer data are given by Doornbos et al. (2010).
109   For the estimation of the thermospheric winds we make use of the measured acceleration
110   components. Under the assumption that the experienced acceleration, $\boldsymbol{a}$, is aligned with the velocity,
111    $\boldsymbol{v}$, with respect to the air rest frame we may write for the vector components:

$$\frac{a_y}{a_x} = \frac{v_y}{v_x} \qquad\qquad (2)$$

112   where the x component is aligned with the spacecraft along-track axis and y with the cross-track
113   axis. Vertical wind contributions are ignored because they are much weaker than the horizontal ones.
114   Since CHAMP had a polar orbit, the zonal wind velocity, u, can be derived by

$$u = v_x\frac{a_y}{a_x}-v_{cor} \qquad\qquad (3)$$

115   where v_x is the orbital velocity (7.6 km/s) and v_{cor} is the corotation velocity of the atmosphere (~490
116   km/s at the equator). The approach actually used for deriving the zonal wind is more sophisticated
117   and is described by Doornbos et al. (2010).
118
119
120   **3. Gross features of thermospheric mass density**
121
122   Before looking into the coupling between ionosphere and thermosphere we present gross
123   features of the quiet time thermosphere. CHAMP crosses all latitudes on its orbit and covers all local
124   times within 4 months. Thanks to the long and homogeneous set of accelerometer measurements the
125   climatology of the mass density at an altitude of 400 km was compiled. Since the CHAMP orbit
126   decays slowly, the actual density readings, $\rho(h)$, have been normalised to a common altitude of 400
127   km ($\rho(400km)$). For this purpose we made use of collocated mass density predictions of the MSIS
128   model.

$$\rho(400km) = \rho(h)\frac{MSIS(400km)}{MSIS(h)}$$

130   This approach is regarded justified since the height change of CHAMP during the studied periods
131   was less than one scale height (~60km).
132   Based on these density data important features were identified by Lui et al. (2005). A
133   quantitative description of the low-latitude thermospheric density and its variation with local time
134   and season was given later by Müller et al. (2009). They also looked into the response to changes in
135   solar EUV flux and magnetic activity. One of their conclusions is that the effects of the four
136   controlling parameters considered in the study, local time, season, solar flux, and magnetic activity,
137   on the thermospheric density can be treated as a linear combination of the different influences. Non-
138   linear coupling was not identified as an important process.
139   In a statistical survey of the thermospheric mass density, Lui et al. (2005) determined among
140   others the mean diurnal variation. Opposed to previous studies, they binned the density readings by
141   magnetic latitude rather than geographic latitude. As can be seen in Figure 2, largest densities are
142   observed about 1.5 hours after noon. Peak values, however, do not appear at the subsolar point, but
143   at latitudes some 25° north and south of the magnetic equator. This is an unexpected phenomenon.

144 For comparison, the thermospheric density distribution as predicted by the MSIS model (Hedin,
145 1991) is shown below. Although gross features are well reflected by the model, there is no sign of a
146 bifurcation at day time hours. Liu et al. (2007a) had a closer look at the so-called equatorial mass
147 density anomaly (EMA). They find that, especially during equinox seasons, the two bands of
148 enhanced density follow reasonably well magnetic latitudes, as can be seen in Figure 3. In addition
149 there is some longitudinal structure visible. This can be related to tidal signatures, as was shown later
150 by Lui et al. (2009b), but this topic will not be addressed here. During solstice seasons the EMA
151 becomes asymmetric, favouring the summer hemisphere (Liu et al., 2007a). There have been
152 attempts to link the EMA with the well-known equatorial ionisation anomaly (EIA). A possible
153 mechanism for causing the density bulges at low latitudes is chemical heating. Following the
154 suggestions of Fuller-Rowell et al. (1997), oxygen ions, O^+, are lifted up over the magnetic equator
155 by the ion fountain effect, then diffuse down along field lines into the northern and southern
156 hemisphere. At E region altitude, charge exchange, in particular between O^+ and O_2^+, takes place.
157 The difference in ionisation energy (1.6 eV per nucleus) is emitted, thus heats and may lift the
158 atmosphere at footprint latitudes of the EIA fluxtubes. However, there are also other processes
159 discussed. A final verification of the EMA mechanism is still pending. In any case, the equatorial
160 mass density anomaly is a product of ionosphere-thermosphere coupling. Plasma is the medium to
161 communicate the magnetic geometry to the neutral gas.
162
163
164 **4. Gross features of thermospheric winds**
165
166 As mentioned in the earlier sections, CHAMP measurements provide also information on
167 thermospheric winds. For these studies altitude changes of the orbit have not been taken into account
168 since it is known that the wind above 300km depends little on altitude (Prölss, 2004). A first global
169 survey of CHAMP low-latitude zonal wind was presented by Liu et al. (2006). They determined the
170 diurnal variation of wind speed and its dependence on solar flux level and magnetic activity.
171 Previously known features could be confirmed: westward wind at the equator at day time and
172 eastward winds during evening and night hours. In a follow-on study Liu et al. (2009a) investigated
173 the zonal wind distribution within the latitude range ±60° of magnetic latitude. As can be seen in
174 Figure 4, highest wind speeds are observed at the equator. The reversals of wind direction do not
175 take place simultaneously at all latitudes. The switch from westward to eastward in the afternoon
176 occurs about an hour later at the equator than at 60° latitude. An even larger time difference of up to
177 7 hours is found in the early morning between equator and 60° latitude for the direction change from
178 eastward to westward. The observed latitude dependence of the zonal wind direction reversal on
179 local time can be explained in part by the influence of the Coriolis force. If an air parcel is moved
180 from the equator to the pole, it is deflected eastward. This situation, valid on the day side, causes the
181 earlier eastward turning at high latitudes around noon. Conversely, air moving from the poles to the
182 equator, as happens on the night side, experiences a westward deflection. Since wind speeds are
183 larger on the night side than on the day side, the Coriolis effect here causes a larger delay between
184 high and low latitude reversals.
185 From Figure 4 it is obvious that highest eastward wind speeds of about 150 m/s are observed
186 at the night time magnetic equator. In order to investigate this situation further Lui et al. (2009a)
187 have looked at the longitude distribution of the zonal wind velocity. As can be seen in Figure 5, there
188 is a jet stream of fast zonal wind along the magnetic equator at all longitudes. Liu et al. (2009a) have
189 explained this high-speed channel by the reduced ion air drag within the equatorial ionisation trough.
190 In that sense the wind distribution controlled by the geomagnetic field geometry is another form of
191 ionosphere-thermosphere coupling.
192 When integrating the zonal wind velocity over all longitudes, as shown in Figure 4, we obtain
193 the net zonal motion of the air at given latitudes. From the right frame of Figure 4 we see that the air
194 rotates faster than the planet at low latitude and slower at high latitude. For an outside observer the

195 Earth's upper atmosphere exhibits a differential rotation velocity, fastest at the equator and
196 progressively slower towards the poles. The excess rotation rate at the equator is 8% according to
197 Figure 4.
198   An even stronger interaction between ions and neutrals is observed at high magnetic
199 latitudes. The wind distribution in the polar region, as observed by CHAMP, was first studied by
200 Lühr et al. (2007). A similar study based on DE-2 satellite data was presented by Thayer et al.
201 (1987). Due to the short DE-2 mission duration and sparse sampling, detailed features could not be
202 resolved. A common result of both studies is the strong day-to-night wind over the polar cap with
203 speeds in excess of 600 m/s. In this region hydrodynamic forces and plasma drifts are well aligned.
204 From comparison with the low-latitude evening terminator region we can expect velocities up to 150
205 m/s due to neutral forcing (see Fig. 4), such as the pressure gradient. A much larger effect has to
206 come from the cross-polar cap potential difference which drives the plasma into the anti-sunward
207 direction at speeds of more than 1 km/s. The plasma drift velocity, v, at CHAMP altitude is
208 described by $v = ExB/B^2$. For a typical polar cap electric field strength of $E = 50$ mV/m and an
209 ambient magnetic field, $B = 50000$ nT, we obtain a plasma velocity, $v = 1$ km/s. Plasma transfers
210 momentum to the neutral particles by collisions. The relevant momentum equation can be written as
211 $\qquad\qquad \rho \, du/dt = -gradP + \rho \, v_{i,n} \, (v - u)$ $\qquad\qquad\qquad\qquad$ (4)
212 where ρ is the mass density, u is the wind velocity, P is the thermal pressure and $v_{i,n}$ is the
213 ion/neutral collision frequency. This equation tells us that the acceleration of wind speed by the
214 plasma is proportional to the collision frequency and to the velocity difference between ions and
215 neutrals. Due to the large inertia of the thermosphere the wind speed will respond to changes in
216 plasma drift with a time delay of tens of minutes.
217   The average polar region wind distribution for the four months around June solstice 2003 is
218 shown in Figure 6. At both hemispheres we observe similar distributions. Signatures are clearer and
219 winds are stronger in the northern (summer) hemisphere. This can be attributed to the higher plasma
220 and neutral densities during that season, giving rise to a higher collision frequency and thus causing
221 a closer coupling between ions and neutrals. There is a clear asymmetry between the dawn and dusk
222 sides. Lühr et al. (2007) report fast winds towards the night time sector on the dawn side, but
223 stagnant flow on the dusk side. There are two effects contributing to this difference. One is the
224 plasma flow along the auroral oval streaming generally sunward. This moves in opposite direction to
225 the prevailing thermospheric wind. The other effect is caused by a combined action of Coriolis and
226 centrifugal forces. For an explanation of the fast day-to-night winds on the dawn side, Lühr et al.
227 (2007) refer to the arguments of Fuller-Rowell and Rees (1984) who state that particles starting at
228 noon and moving westward experience an equatorward centrifugal force, but at the same time a
229 poleward Coriolis force. The velocity at which the two forces cancel each other depends on the polar
230 distance, θ
$\qquad\qquad \sin\theta = v/985$ [m/s] $\qquad\qquad\qquad\qquad\qquad\qquad$ (5)
231
232 At a latitude of 60° ($\theta = 30°$) we obtain $v = 498$ m/s for the critical velocity. This value is close to the
233 wind speed observed on the dawn side (cf. Fig. 6). Obviously, many air particles move along the
234 stable paths and the counter-streaming plasma has little effect. On the dusk side the Coriolis and
235 centrifugal forces act into the same direction deflecting the particles into an anti-cyclonic spiral
236 motion. Such a signature can be seen in Figure 6 near 70° of magnetic latitude at 18:00 local time.
237 The additional effect of a sunward plasma flow along the auroral oval causes wind stagnation on the
238 afternoon side.
239   Within the night sector the equatorward wind is deflected westward, as expected from the
240 action of the Coriolis force. This observation is consistent with our interpretation of the latitude
241 dependent shift in local time, where the zonal wind switches direction, as evident from Figure 4.
242   The effect of the high-latitude plasma drift pattern on thermospheric winds was investigated
243 in more details by Förster et al. (2008). The authors clearly show that the wind direction over the
244 polar regions depends on the interplanetary magnetic field (IMF) components B_y and B_z. Their

245 results provide further evidence for the close control of the plasma dynamics on the thermospheric
246 wind. Over the northern hemisphere polar cap highest wind speeds are observed for a combination of
247 negative IMF B_y and B_z components. In the southern hemisphere wind speeds maximise for positive
248 IMF B_y and negative B_z. The clockwise wind vortex on the dusk side increases in the northern
249 hemisphere when IMF B_y is positive. The opposite B_y polarity causes the vortex to grow in the south.
250 This behaviour is consistent with the response of the plasma vortex to IMF conditions. Interestingly,
251 on the dawn side the wind velocity shows little dependence on IMF orientation. Obviously, the
252 coupling between ions and neutrals is less efficient here. For a dedicated investigation of the
253 interaction between neutral air and plasma in the F region, it would be desirable to measure wind and
254 ion drift by the same spacecraft. ESA's upcoming constellation mission "Swarm" will provide this
255 capability; it carries both an accelerometer and an ion driftmeter on each of the three spacecraft.
256
257

258 ## 5. The cusp-related mass density anomaly

259
260   In section 3 we had presented the average thermospheric mass density at low and mid
261 latitudes for altitudes around 400 km. Here we focus on local phenomena at high magnetic latitudes.
262 A surprising observation, made already early in the CHAMP mission, was the appearance of rather
263 localized large peaks in air drag. As an example, acceleration measurements over the first 8 orbits on
264 25 September 2000 are shown in Figure 7. Clearly visible are the harmonic variations of air drag
265 over an orbit. Near the orbital maxima there are large small-scale spikes in deceleration. All these
266 peaks tend to appear at magnetic latitudes near 75° and within the time sector around 10:30 of
267 magnetic local time (MLT). This confinement in local occurrence suggests a relation to the
268 ionospheric cusp. Lühr et al. (2004) were the first to look into this phenomenon in some detail. They
269 related the deduced local mass density enhancement to concurrent peaks in ionospheric current
270 observations. During the prominent event shown in Figure 8 the air density almost doubles in the
271 cusp region with respect to the background. Collocated with the density peak intense field-aligned
272 currents (FACs) are observed. A particularly outstanding feature is the strong burst of kilometre-
273 scale FACs. Also the Hall current in the electrojet region is enhanced. Both FAC and electrojet
274 intensities are deduced from the CHAMP high-resolution magnetic field measurements. The
275 approach applied for deriving these currents is described by Wang et al. (2005) and Ritter et al.
276 (2004) for the FAC and electrojet, respectively. After CHAMP has crossed the polar cap we find on
277 the same pass comparably strong Hall currents in the evening auroral region, but they are not
278 accompanied by a density anomaly. Lühr et al. (2004) provided additional evidence that intense
279 small-scale FACs play an important role for the formation of cusp-related density anomalies.
280   A more extended study of this density phenomenon was performed by Schlegel et al. (2005),
281 but no conclusive explanations for a generation mechanism could be offered. Demars and Schunk
282 (2007) made an attempt to reproduce the density anomaly by means of their high-resolution
283 thermosphere model. For achieving a local doubling of the mass density near the cusp, as reported
284 by Lühr et al. (2004), they had to increase the heating in the E region by an unrealistic factor of
285 greater than100.
286   Motivated by these open issues Rentz and Lühr (2008) performed a systematic study of the
287 cusp-related density anomaly, based on CHAMP data from the years 2002-2005. An anomaly is
288 defined as an enhancement above the large-scale background density. It is quantified either as an
289 absolute increase above background or as a relative enhancement. The region scanned comprises the
290 magnetic local time sector 08 to 16 MLT and the latitude range of 60° to 80° of magnetic latitude in
291 both hemispheres. The peak value of density enhancement from each overflight was sorted into the
292 appropriate equal-area bin of a latitude-by-local-time grid. Figure 9 shows the resulting average
293 amplitude distribution on a dial plot separately for every year. Density anomalies cluster around the
294 nominal cusp location in all cases. The amplitudes get smaller each year and decrease by a factor of
295 4 from 2002 to 2005. This is accompanied by a reduction of solar EUV flux. The mean F10.7 index

296 declines from 181 sfu in 2002 to 91 sfu in 2005. This suggests a significant dependence of the
297 density anomaly's magnitude on solar activity. Similar results, as shown for the northern
298 hemisphere, are observed in the south, but there the amplitudes are smaller by a factor of 1.7 on
299 average.
300   In the quest for the mechanism that causes the mass density enhancement near the cusp Rentz
301 and Lühr (2008) correlated the anomalies with solar flux and solar wind parameters. The solar wind
302 input is characterised by the merging electric field, E_m, as defined by Kan and Lee (1979)
303

$$E_m = v_{SW} \sqrt{B_y^2 + B_z^2} \, \sin^2\left(\frac{\theta}{2}\right) \tag{6}$$

305 where B_y and B_z are the IMF components, v_{sw} is the solar wind speed, and θ is the IMF clock angle
306 ($\tan\theta = \dfrac{B_y}{B_z}$). The solar EUV input is quantified by $P10.7 = 0.5 \ (F10.7 + aF10.7)$ where $aF10.7$ is
307 the average of F10.7 over 81 days. Figure 10 shows the dependence of the anomaly amplitude on
308 P10.7 and E_m. From the top two frames we may conclude that a combination of high solar flux with
309 strong solar wind input favours the formation of large density peaks. For this reason we find
310 anomalies with appreciable amplitude only in the upper right corner. The reduced amplitude of the
311 anomalies in the southern hemisphere, as quantified above, is clearly visible in this figure.
312   Beside the absolute amplitude, also the relative amplitude of the anomaly with respect to the
313 background density is shown in Figure 10 (lower frames). In that case the dependence on solar EUV
314 is largely reduced but not fully removed. In any case, it demonstrates the dominant role of the solar
315 wind input for the formation of the anomalies.
316   A prime question that remains after all is, what causes the confinement of the anomalies to
317 the ionospheric cusp region? For part of the answer we can refer to the association with the intense
318 bursts of small-scale FACs as shown by Lühr et al. (2004). It had been reported by Neubert and
319 Christensen (2003) and later by Rother et al. (2007) that there exists a clear occurrence maximum of
320 kilometre-scale FACs in the polar cusp region. With respect to the model results obtained by Demars
321 and Schunk (2007), however, it was questionable whether the amount of Joule heating in the E
322 region caused by small-scale FACs would be sufficient to fuel the observed amount of air up-
323 welling.
324   Rentz and Lühr (2008) suggested that particle precipitation may also play an important role
325 for the formation of the density anomaly. In order to test the hypothesis we may have a look at the
326 important quantities. The effective amount of Joule heating can be expressed as function of altitude
327

$$\boldsymbol{j}\cdot\boldsymbol{E} = \sigma_P(h)\, E^2 = \sigma_P(h)\, (E_{DC} + E_{AC})^2 \tag{7}$$

328 where $\boldsymbol{j}$ is the local current density, $\boldsymbol{E}$ is the electric field and E_{DC}, and E_{AC} are the large- and small-
329 scale parts of the electric field, $\sigma_P(h)$ is the height-dependent Pedersen conductivity. The E-field
330 depends only weakly on altitude because the almost vertical magnetic field lines can be considered
331 as equipotential lines. For a given electric field the Pedersen conductivity determines the amount of
332 Joule heating and the affected altitude range. For assessing the effect of precipitation on the
333 conductivity we make use of the CTIP model (Millward et al., 1999), since there are no particle
334 measurements from CHAMP. It is known that the cusp is characterised by high fluxes of soft
335 particle precipitation. Typical energies for particles have been used, Maxwellian distributions
336 peaking at 50 eV for electrons and 500 eV for ions. Geophysical conditions were chosen as those on
337 14 December 2002. CTIP runs were compared for precipitation switched on and off. Figure 11
338 presents results of the two runs. Height profiles of the Pedersen conductivity show a clear response
339 to the precipitating particles. For altitudes between 130 and 400 km the conductivity is significantly
340 enhanced by precipitation. When looking at the relative increase of conductivity (plotted in the right
341 frame), which is proportional to the ratio of the Joule heating rate with and without precipitation, we

7

find the largest effects up to a factor of 9 above 150 km altitude, i.e. in the F1 region. This uplift of the conductive and current-carrying layer is caused by high fluxes of low energetic particles which is a typical feature of the cusp. Particle precipitation in the cusp is primarily caused by reconnection at the dayside magnetopause. The strength of the merging electric field, E_m, is commonly seen as an indicator of an enhanced reconnection rate. In this respect E_m seems to indicate a two-fold effect on the strength of the cusp-related density anomalies: (1) reconnection on the dayside controls the flux of precipitating soft particles, (2) merging enhances the convection electric field which is partly mapped into the cusp region. It has been noticed earlier from Freja and FAST satellite data that high fluxes of cusp-type soft precipitation are commonly accompanied by intense small-scale FACs. Waterman et al. (2009) provided observational evidence for this by comparing DMSP particle precipitation measurements with FAC estimates from Ørsted and CHAMP. Another particular feature is the strong conductivity enhancement above 150 km of altitude. This causes a large fraction of currents to flow in the F1 region. In this altitude range the thermospheric density is about two orders of magnitude lower than in the E region at 110 km. This means, a given amount of Joule heating will cause a much larger temperature enhancement in the F1-layer than in the E-layer.

By summarizing the observations made in the context of mass density anomalies we may offer a suggestion why prominent density peaks occur preferably in association with the ionospheric cusp. The intense precipitation of low energy particles is regarded as the key process for determining the location of the anomaly. Some researchers even claim that the energy deposited by the incident particles may already account for the major part of heating (Clemmons et al., 2008). Soft precipitation occurs frequently in the cusp region. The largely enhanced conductivity in the F1 region due to precipitation places the heating region to 150 km and higher. At this altitude predominantly molecules are heated and subsequently uplifted. Crowley et al. (2008) presented observational evidence for a reduced O/N_2 ratio in the cusp/cleft region during enhanced magnetic activity. This increased abundance of heavier particles in the upper thermosphere adds to the density anomaly detected by CHAMP. Our suggested mechanism is also consistent with the strong dependence of the anomaly amplitude on the merging electric field. The merging rate controls both the precipitating particle flux and the cross-polar cap potential. A verification of this chain of arguments by physics-based numerical modelling would be highly desirable.

6. Substorm effects on the thermosphere

In their early paper Liu et al. (2005) reported about a mass density anomaly observed by CHAMP at auroral latitudes in the time sector before midnight. The authors found that the anomaly intensifies during magnetically active periods. From that dependence they suggested a relation between the enhanced air density and substorm processes. In a dedicated statistical study Ritter et al. (2010) investigated the thermospheric response to the substorm onset. CHAMP mass density and wind measurements were investigated for a large number of substorms. The survey was performed using onsets from the catalogue published by Frey and Mende (2006), containing more than 4000 entries. Events were selected based on the criteria that CHAMP passed the onset location sufficiently close in space and time. By stacking the results of many substorm events significant structures in mass density and wind could be deduced.

In order to determine the spatial and temporal evolution of substorm-related thermospheric effects CHAMP data were binned according to certain criteria. Figure 12 shows a local time dial plot with a schematic illustration of the auroral oval. The substorm onset location is marked by a yellow/orange star. There are three local time bins defined, each one is 30° in longitude wide (2 h in LT). When CHAMP passed the actual onset location to the west (0°-30° in longitude) data are sorted into bin 1, when it passed to the east (0°-30° in longitude) data went into bin 2 and further east (30°-60° in longitude) into bin 3. For tracking the temporal evolution of the disturbance the satellite pass

392 before the substorm is taken as reference and is used for comparison with the passes subsequent to
393 the onset. The orbital period of CHAMP is about 93 minutes.
394   Figure 13 shows the mean thermospheric density response to a substorm. Presented are
395 observations of bin 2, around midnight. The left frames contain variations at middle latitudes, and on
396 the right side the high-latitude response is shown. Substorms have a significant effect on the
397 thermosphere during magnetically active periods, as can be seen in the top panels ($K_p \geq 4$).
398 Conversely, for substorms during quiet times ($K_p \leq 2$), we hardly see any difference between the
399 before-substorm curve (black) and the later passes. The amount of energy accumulated in the
400 magnetospheric tail and released into the thermosphere during quiet-time isolated events is
401 obviously too small. For that reason we focus in the subsequent paragraphs on active periods. Figure
402 14 shows mass density changes with respect to the before-substorm measurements. Plotted are mean
403 latitude profiles derived from subsequent orbits. Measurements of the three consecutive passes are
404 taken on average 45 min, 2.4 h and 4 h after the onset. Results of all three local time bins are
405 presented. An outstanding feature is the mass density bulge appearing at the magnetic equator 4 h
406 after the onset. Density changes are largest in bin 2, around midnight. First effects are observed at
407 high latitudes between 70° and 80° of magnetic latitude (red curves). During the second pass (blue
408 curve) the density enhancement has already expanded to mid latitudes, both from the northern and
409 southern auroral regions. By the time of the third pass (green curves), about 4 hours after onset, the
410 substorm-related density enhancements from both hemispheres reach the equator and pile up there.
411 All these effects are largest in the time sector around midnight (bin 2). Here the density bulge at the
412 equator surmounts the background density by 20%. At locations to the west of the onset (bin 1) the
413 same density features are observed, but with smaller amplitude. The apparent minor density bulge of
414 the red curve at the equator in bin 1 is a remnant of a substorm taking place about 3 hours earlier.
415 More details of this study can be found in Ritter et al. (2010). Interestingly, in the post-midnight
416 sector (bin 3) only marginal substorm-related thermospheric variations are recorded. The amplitudes
417 are in the range of uncertainties ($\pm 0.1 \cdot 10^{-12}$ kg/m^3). This asymmetry between pre- and post-midnight
418 effects supports the notion of the widely accepted current wedge model (e.g. Clauer and Mc Pherron,
419 1974; Ritter and Lühr, 2008) according to which most of the energy injected from the tail is
420 deposited in the vicinity of the upward directed field-aligned current region in the pre-midnight
421 sector.
422   The density enhancement caused by the substorm in the auroral region propagates as
423 travelling atmospheric disturbance (TAD) equatorward. Ritter et al. (2010) have deduced a mean
424 propagation speed of 650 m/s from their observations. Furthermore they report a westward
425 deflection of the travel path. This can largely be explained by the Coriolis force acting on the air
426 parcel which moves equatorward, but an additional westward velocity component is needed for the
427 full explanation of the observations. From these results we see that auroral phenomena like
428 substorms can affect the thermosphere at low and mid latitude significantly.
429   Substorms are expected to have also an influence on thermospheric winds. In order to check
430 that, Ritter et al. (2010) had a look at zonal winds which are detectable by CHAMP. The same
431 procedure as used for the density study was applied to the cross-track wind component. Figure 15
432 shows the obtained average zonal wind distribution observed in association with substorms. In
433 general, there is little difference between the various passes before and after the onset both during
434 magnetically active periods (top frames) and quiet periods (bottom frames). This suggests that
435 substorms do not influence the zonal wind on the night side significantly. However, we have no
436 information about effects on the meridional wind. Based on simulation results Fujiwara and Miyoshi
437 (2006) predict a strong equatorward meridional wind surge around midnight which is related to the
438 equatorward TAD initiated by the substorm. For zonal winds their model also predicts only small
439 effects.
440   For both cases of high and low magnetic activity we find peak eastward zonal wind speeds at
441 the magnetic equator and lower velocities at higher latitudes. This signature is consistent with the
442 global zonal wind distribution shown in Figure 4. Interestingly, peak wind velocities are higher

during quiet times. This observation confirms the prediction of the DWM07 model that there is a
westward directed disturbance wind during active periods at low and mid latitude on the night side
(Emmert et al., 2008). The disturbance wind amounts to 20 m/s at the equator and increases
monotonically to 50 m/s at 50° of magnetic latitude. At high latitudes, Ritter et al. (2010) report a
reduction of the westward wind to almost stagnation around 65° of magnetic latitude during high
magnetic activity. In order to find an explanation for the wind speed reduction we estimated the
electrojet strength in this region from CHAMP magnetic field data. Ritter et al. (2004) described and
validated in a systematic study their approach for determining source-free currents (largely identical
with the auroral electrojet) from CHAMP total magnetic field recordings. We applied this technique
to magnetic field data from the same set of CHAMP passes as used in connection with our substorms
study. Figure 16 shows the latitudinal distribution of the electrojet current density as derived from a
superposed epoch analysis applied to many substorms. Again magnetically active and quiet periods
were considered separately. Also the colours of the curves mark the same succession of orbits after
onset. In both frames we find negative (westward) electrojet currents at latitudes where the westward
wind is diminished. Since the plasma drifts in the opposite direction as the electrojet current, we can
imply eastward flowing plasma in the latitude range of electrojet. This can explain neatly the
retarding effect on the westward wind by ion friction through eastward drifting plasma.

When looking at the evolution of the electrojet strength over the course of a substorm we find
a persistent westward electrojet before and well after the substorm. This seems to be driven by the
prevailing convection electric field. An outstanding feature can be observed at the first orbit ($\sim$ 45
min) after the onset (red curve). There we find a current strength increase on average by a factor of
1.5, which is attributed to the substorm-related current wedge (see Ritter and Lühr, 2009).
Interestingly, this additional current does not seem to have an influence on the zonal wind. This
observation implies that there is no enhancement of the electric field (plasma drift) by the substorm,
just an increase in conductivity. The highly conductive channel appears a few degrees further
poleward of the prevailing electrojet. This interesting behaviour of the substorm electrojet justifies
further investigations including concurrent plasma drift measurements.

7. The equatorial F region dynamo

In the previous sections we presented examples for thermospheric signatures caused by plasma
processes. Here we show a case of an ionospheric process driven by the thermosphere. The concept
of an F region dynamo was presented already several decades ago by Rishbeth (1971). He suggested
a wind-driven dynamo in the low-latitude ionospheric F region. Zonal wind blowing across the
geomagnetic field will cause a charge separation by interaction with the plasma. This sets up a
polarisation electric field in the meridional plane. The strength of the E-field, E, driven by the F
region dynamo depends on the ratio between the conductance in the F and E regions. According to
Kelley (2009) it can be expressed as

$$E = \frac{\Sigma_P^F}{\Sigma_P^{EN} + \Sigma_P^{ES} + \Sigma_P^F} \; uxB \tag{8}$$

where Σ_P^{EN} and Σ_P^{ES} are E region height-integrated Pedersen conductivities at the northern and
southern ionospheric footprints, Σ_P^F is the fluxtube-integrated conductivity in the F region, u is the
wind velocity, and B is the ambient magnetic field. The F region electric field drives toroidal current
systems in both hemispheres. Figure 17 shows schematically the important elements of the F region
dynamo in the evening sector.

First observational evidence of the F region dynamo was presented by Maeda et al. (1982)
based on Magsat data. Since that satellite was in orbit only for a few months and sampled only the

491   dawn/dusk sector, many issues were left unresolved. New opportunities for studying this
492   phenomenon arose with the CHAMP mission lasting for almost one solar cycle. The diurnal
493   variation of the F region dynamo current strength was first presented by Lühr and Maus (2006).
494   They found downward currents in the F region which peak around noon and upward currents in the
495   evening that are largest between 18 and 19 local time. This notion is consistent with prevailing
496   westward zonal winds during daytime and eastward winds in the evening and night time hours (see
497   section 4).
498   A detailed statistical study based on CHAMP data for determining the climatological
499   characteristics of the F region dynamo was conducted by Park et al. (2010a). The authors sorted the
500   data by various parameters and thus could determine the dependence of the current strength on local
501   time, season, longitude and solar flux. Figure 18 shows the local time variation of the sheet current
502   density generated by the F region dynamo. Downward vertical currents are denoted positive. The
503   diurnal variations are determined separately for each season. During post-midnight and morning
504   hours no clear current signal could be deduced from the magnetic field measurements. Consistent
505   with the results of Lühr and Maus (2006) Park et al. (2010a) find downward (positive) currents in all
506   seasons around noon and upward (negative) current densities around evening hours. In the vicinity
507   of the current reversal our automatic processing does not work properly. Therefore, the unreliable
508   results in this area have been omitted in Figure 18. Nevertheless, a zero crossing of the current
509   between 15 and 16 LT can be found for all seasons. This local time is consistent with the reversal in
510   zonal wind direction from westward to eastward (see Fig. 4). Smallest current densities are attainted
511   around June solstice, while during equinox and December solstice months the diurnal variations are
512   comparable and amplitudes are about twice as large as in June.
513   The vertical current in the F region is diverted and flows along field lines into the E regions
514   of both hemispheres. For the closure currents, J_P, in the E-layer we obtain

$$J_P = \Sigma_P^E \, E \tag{9}$$

515   where E in this case is the sum of E and F region electric fields. When inserting the electric field
516   from Equation (8) into Equation (9) and assuming that the conductance, Σ_P^E, is the same in the two E
517   regions and that the conductance in the E region is much larger than that in the F region, which is
518   reasonable during day time, we obtain

$$J_P = \tfrac{1}{2} \Sigma_P^F [uB]^F - \Sigma_P^E [uB_z]^E \tag{10}$$

519

520   Here the terms in brackets with superscript F denote the zonal wind velocity and the field strength in
521   the equatorial F region, whereas in the brackets with superscript E we consider the zonal wind and
522   vertical magnetic field at the E region footprint of the fluxtube. Equation (10) reveals that the sheet
523   current density in the E region depends on the zonal winds in the E and F regions. Around noon the
524   zonal winds at the two layers have, according to the wind model HWM07, opposite directions, and
525   the product (uxB) is about 5 times larger in the F region than in the E-layer. Thus, J_P is the sum of
526   two almost equally strong contributions from both layers. However, the vertical F region dynamo
527   current, J_Z, is less influenced due to the small E region electric field contribution.

$$J_Z \approx \Sigma_P^F \left\{ [uB]^F - [uB_z]^E \right\} \tag{11}$$

528

529

530   From Equation (11) we can see that the current of the F region dynamo is strongly controlled by the
531   fluxtube-integrated conductivity in the F region. This quantity is highly dependent on the electron
532   and neutral particle density. For the interpretation of the current strength minimum around June
533   solstice one has to look into the electron density (Lui et al., 2007b) and neutral density (Müller et al.,
534   2008). Both exhibit their annual minimum during that season. The reported density depletions are
535   sufficient to explain the June depression of the F region dynamo currents.
536   A detailed investigation of the longitudinal variation of the F region dynamo current was
537   performed by Park et al. (2010a). Extracted from that study we show the longitude dependence of
538   the noon-time F region dynamo currents in Figure 19, separately for the seasons. Quite obvious are
539   again the small amplitudes at times around June solstice. During equinoxes there is a remarkable

longitudinal variation of the current strength. Values vary between 2 and 15 mA/m. Rather obvious is a four-peaked longitudinal pattern. This is indicative of forcing by non-migrating tides. We will not go into the details of that topic, but refer to Park et al. (2010a) who discussed the tidal aspect in some depth. During the months around December solstice the current intensity varies not much with longitude. A wavenumber-2 structure seems to dominate. During all seasons an outstanding current feature is observed around 300°E longitude. We relate this prominent peak in F region dynamo current to the South Atlantic Anomaly (SAA). Takeda (1996) predicted that in a region of low ambient magnetic field the F region is lifted higher up. As a consequence, it populates a longer fluxtubes and the field-aligned integrated Pedersen conductivity become larger. The resulting positive effect on the vertical current density (cf. Eq. (11)) is expected to surmount that of the reduced polarisation field, uxB. Our observations are in support of Takeda's (1996) results.

Quite different longitudinal variations were observed during evening hours. In this local time sector several features of the noon-time recordings are missing. From Figure 20 it can be deduced that the current distribution is less structured. There is no outstanding current density peak near the SAA (around 300° longitude). Also the wavenumber-4 longitudinal pattern has disappeared. In particular, during equinoxes there is only little variation with longitude. For June solstice months we observe very week F region dynamo currents over the longitude sector 300° – 108°E. In other regions they attain appreciable values, peaking around 230°E of longitude. Similarly, during December solstice months we find a large-scale variation with minimum around 150°E and maximum at 320°E of longitude. The observed phase difference of the dominating wavenumber-1 longitudinal variation between the two solstices is, according to Park et al. (2010a), 115°E in longitude. This large-scale variation of the vertical F region current density can be attributed to the combined effects of the longitude-dependent displacement of the dip-equator from the geographical equator and the seasonal variation of upper atmospheric conditions.

In general, we can state that the F region dynamo currents around noon reflect many features of the E region dynamics, e.g. wavenumber-4 longitudinal pattern and SAA enhancement. All these do not appear in the recordings from the evening hours' F region dynamo. This confirms the strong coupling between E and F region during day time and the disconnection of the regions at sunset. Further studies are required to resolve all the different longitudinal variations of the F region dynamo.

Another influence that has been investigated by Park et al. (2010a) is the dependence on the solar flux index, F10.7. According to Equation (11) the F region dynamo current is directly proportional to the conductance in the F region. The conductance depends both on electron density and neutral particle density. These two quantities increase with the solar flux at F region heights, as has been shown for the neutral density, e.g. by Müller et al. (2009) and for the electron density in the equatorial ionisation anomaly, e.g. by Stolle et al. (2008). Figure 21 presents the dependence of the F region dynamo current density on the solar flux level, as observed by CHAMP, separately for data taken around noon and during evening hours. For both time sectors we find a clear linear relation. Interestingly, the fitted regression lines have practically the same slopes. The noon values, however, are consistently higher by about 1mA/m. Such an amplitude difference is also evident in Figure 18. The similarity in slope around noon and dusk suggest that the same mechanisms cause the F region dynamo currents to increase in response to higher solar flux. As mentioned before, a more conductive F region is our preferred candidate.

It has been suggested for quite some time that the F region dynamo in the dusk sector might be the main driver for the peak in vertical plasma drift around sunset. Park at al. (2010b) were the first to provide observational evidence, based in CHAMP data, for the close relationship between the F region dynamo current strength and the peak value of the vertical plasma drift during the pre-reversal enhancement (PRE). They also show that the azimuthal conductivity gradient of the E-layer along the terminator is an important factor in this relationship. Since the peak plasma drift during PRE plays a crucial role for initiating ionospheric instabilities during pre-midnight hours, a better

understanding of the dusk-sector current generator is of great interest. Further studies on the relation between F region dynamo and PRE are thus highly recommended.

8. Conclusion and Outlook

The previous sections gave an idea of the large variety of processes coupling the ionosphere with the thermosphere. The German satellite, CHAMP, with its continuous measurements over almost one solar cycle helped to advance our understanding of many phenomena. In the past, progress in research was often hampered by the lack of sufficient observations of thermospheric quantities. This has changed drastically since satellites like CHAMP and GRACE carry sensitive accelerometers for recording the air drag. Only now it has become clear that thermospheric density distribution is significantly controlled by the shape of the geomagnetic field. Examples for that are found at low latitudes, e.g. the equatorial mass density anomaly, and at high latitudes, e.g. the cusp-related density enhancement. Both these features are not reproduced by any of the thermospheric models. Since these are systematic features, their consideration in models is highly recommended.

Ionospheric processes at auroral latitudes have been shown to have strong effects on the thermospheric dynamics. This connection is known qualitatively since the early days of satellite missions. Only now, statistically significant quantitative relations between plasma dynamics and thermospheric response have been deduced. An example presented here is the thermospheric wind at polar regions. It is driven strongly by plasma convection, but shows also a clear response to Coriolis force and centrifugal force. Therefore, plasma convection and polar region wind show rather different patterns. Also in this case, empirical models provide only a rather poor representation of wind patterns at high latitudes. Another example is the thermospheric disturbance caused by substorms. CHAMP measurements revealed that air parcels lifted up at auroral latitudes propagate as density bulges equatorward and cause large transient density enhancements at low latitude. Zonal winds are only marginally influenced by substorms.

The equatorial F region dynamo is presented, as an example of a ionospheric process driven by the thermosphere. Here again, CHAMP measurements provide the first comprehensive overview of its properties. Features of the F region dynamo in the noon sector reflect many properties of the E region dynamics. This is indicative of a close connection between E and F regions during that time of the day. Conversely, a decoupling of the two regions is deduced from the F region dynamo current features in the dusk sector. On the other hand, we found a close relation between the F region current strength in that sector with the vertical plasma drift velocity during the pre-reversal enhancement (PRE). This result suggests that the size of the PRE, which plays an important role for post-sunset ionospheric instabilities, is controlled by a wind-driven dynamo. In particular, this coupling process between neutral particles and plasma calls for further detailed investigations.

ESA's upcoming constellation mission Swarm, consisting of 3 CHAMP-like spacecraft, is well-equipped to advance the studies of ionosphere-thermosphere coupling. With its instrumentation package involving accelerometer, ion driftmeter and magnetometers it will record the ion and neutral dynamics simultaneously. The foreseen orbit configuration of the constellation enables the employment of spatial gradients in the data interpretation. The launch of Swarm is scheduled for July 2012.

References

Clauer, C. R. and McPherron, R. L.: Mapping of local time, universal time development of
    magnetosphere substorms using mid-latitude magnetic observations, J. Geophys. Res., 79, 2812–
    2820, 1974.

Clemmons, J. H., J. H. Hecht, D. R. Salem, and D. J. Strickland (2008), Thermospheric density in
    the Earth's magnetic cusp as observed by the Streak mission, Geophys. Res. Lett., 35, L24103,
    doi:10.1029/2008GL035972.

Crowley, G., A. Reynolds, J. P. Thayer, J. Lei, L. J. Paxton, A. B. Christensen, Y. Zhang, R. R.
    Meier, and D. J. Strickland, (2008) Periodic modulations in thermospheric composition by solar
    wind high speed streams, *Geophys. Res. Lett., 35,* L21106, doi:10.1029/2008GL035745..

Demars, H.G. and R.W. Schunk. Thermospheric response to ion heating in the dayside cusp. *J. of
    Atm. and Sol.-Terr. Phys.*, 69:649–660, 2007.

Doornbos, E, J, van den Ijssel, H. Lühr, M. Förster, G. Koppenwallner, Neutral density and
    crosswind determination from arbitrarily oriented multi-axis accelerometers on satellites, *J.
    Spacecraft, Rockets*, **47**, 580-589, 2010.

Emmert, J. T., D. P. Drob, G. G. Shepherd, G. Hernandez, M. J. Jarvis, J. W. Meriwether, R. J.
    Niciejewski, D. P. Sipler, and C. A. Tepley (2008), DWM07 global empirical model of upper
    thermospheric storm-induced disturbance winds, J. Geophys. Res., 113, A11319,
    doi:10.1029/2008JA013541.

Förster, M., S. Rentz, W. Köhler, H. Liu and S. E. Haaland: IMF dependence of high-latitude
    thermospheric wind pattern derived from CHAMP cross-track measurements, Ann. Geophys.,
    26, 1581-1595, 2008.

Fuller-Rowell, T. J. and Rees, D.: Interpretation of an anticipated long-lived vortex in the lower
    thermosphere following simulation of an isolated substorm, Plant. Space Sci., 32, 69–86, 1984.

Fuller-Rowell, T. J., M. V. Codrescu, B. G. Fejer, W. Borer, F. Marcos, and D. N. Anderson, 1997.
    Dynamics of the low-latitude thermosphere: Quiet and disturbed conditions, *J. Atmos. Terr.
    Phys., 61,* 1533–1540.

Hedin, A. E., Extension of the MSIS thermosphere model into the middle and lower atmosphere, J.
    Geophys. Res., 96, 1159– 1172, 1991.

Kan, J. R., and L. C. Lee, Energy coupling function and solar wind-magnetosphere dynamo,
    Geophys. Res. Lett., *6*, 577–580, 1979.

Kelley, M.C. *The Earth's Ionosphere*, Second Edition, Academic Press, San Diego, 2009.

Liu, H., H. Lühr, V. Henize and W. Köhler, 2005. Global distribution of the thermospheric total
    mass density derived from CHAMP, *J. Geophys. Res., 110,* A04301;
    doi:10.1029/2004JA010741.

Liu, H., H. Lühr, S. Watanabe, W. Köhler, V. Henize and P. Visser, 2006. Zonal winds in the
    equatorial upper thermosphere: Decomposing the solar flux, geomagnetic activity, and seasonal
    dependencies, *J. Geophys. Res., 111,* A07307, doi:10.1029/2005JA011415.

Liu, H., H. Lühr, and S. Watanabe, (2007a). Climatology of the equatorial thermospheric mass
    density anomaly, *J. Geophys. Res.,* 112, A05305, doi:10.1029/2006JA012199.

Liu, L., B. Zhao, W. Wan, S. Venkartraman, M.-L. Zhang, and X. Yue (2007b), Yearly variations of
    global plasma densities in the topside ionosphere at middle and low latitudes, J. Geophys. Res.,
    112, A07303, doi:10.1029/2007JA012283.

Liu, H., S. Watanabe, T. Kondo, 2009a. Fast thermospheric wind jet at the Earth's dip equator,
    Geophys. Res. Lett., 36, L08103doi:10.1029/2009037377.

Liu, H., M. Yamamoto, H. Lühr, 2009b. Wave-4 pattern of the equatorial mass density anomaly- A
    thermospheric signature of tropical deep convection, *Geophys. Res. Lett., 36,* L18104,
    doi:10.1029/2009GL039865.

Lühr, H., M. Rother, W. Köhler, P. Ritter, L. Grunwaldt, 2004. Thermospheric up-welling in the cusp region, evidence from CHAMP observations, *Geophys. Res. Lett.,* 31, L06805, doi:10.1029/2003GL019314.

Lühr, H. and S. Maus, 2006. Direct observation of the F region dynamo currents and the spatial structure of the EEJ by CHAMP, *Geophys. Res. Lett.,* 33, L24102, doi:10.1029/2006GL028374.

Lühr, H., S. Rentz, P. Ritter, H. Liu and K. Häusler, Average thermospheric wind patterns over the polar regions, as observed by CHAMP, *Ann. Geophys.,* **25,** 1093-1101, 2007.

Maeda, H., T. Iyemori, T. Araki, and T. Kamei, 1982. New evidence of a meridional current system in the equatorial ionosphere, Geophys. Res. Lett., 9, 337– 340.

Müller, S., H. Lühr, and S. Rentz, 2009. Solar and magnetospheric forcing of the low latitude thermospheric mass density as observed by CHAMP, *Ann. Geophys.,* 27, 2087–2099.

Neubert, T., and F. Christensen (2003), Small-scale, field-aligned currents at the top-side ionosphere, Geophys. Res. Lett., 30(19), 2010, doi:10.1029/ 2003GL017808.

Park, J., H. Lühr, K.W. Min (2010), Characteristics of F-region dynamo currents deduced from CHAMP magnetic field measurements, *J. Geophys. Res., 115*, A10302, doi:10.1029/2010JA015604.

Park, J., H. Lühr, B.G. Fejer, and K.W. Min (2010), Duskside F-region dynamo currents: its relationship with prereversal enhancement of vertical plasma drift, *Ann. Geophys., 28*, 2097–2101, 2010b.

Prölss, G. W,. *Physics of the Earth's Space Environment,* Springer, Berlin, 2004

Reigber, C., H. Lühr, and P. Schwintzer, 2002. CHAMP mission status, *Adv. Space Res.,* 30(2), 129-134.

Rentz, S. and H. Lühr, 2008. Climatology of the cusp-related thermospheric mass density anomaly, as derived from CHAMP observations, *Ann. Geophys., 26,* 2807-2823.

Rishbeth, H., 1971. The F-layer dynamo, *Planet. Space Sci., 19*, 263–267.

Ritter, P., H. Lühr, A. Viljanen, O. Amm, A. Pulkkinen, and Sillanpää, Ionospheric currents estimated simultaneously from CHAMP satellite and IMAGE ground-based magnetic field measurements: A statistical study at auroral latitudes, *Ann. Geophys.,* **22,** 417-430, 2004.

Ritter, P. and H. Lühr (2008), Near-Earth magnetic signature of magnetospheric substorms and suggestions for a new substorm current model, *Ann. Geophys., 26,* 2781-2793, 2008.

Ritter, P., H. Lühr, and E. Doornbos, Substorm-related thermospheric density and wind disturbances derived from CHAMP observations, *Ann. Geophys., 28,* 1207-1220, 2010.

Rother, M., K. Schlegel, and H. Lühr, CHAMP observation of intense kilometre-scale field-aligned currents, evidence for an Alfvén resonator, *Ann. Geophys.,* **25,** 1603-1615, 2007.

Schlegel, K., H. Lühr, J.-P. St.-Maurice, G. Crowley, and C. Hackert, Thermospheric density structure over the polar regions observed with CHAMP, *Ann. Geophys.,* **23,** 1659-1672, 2005.

Stolle, C., C. Manoj, H. Lühr, S. Maus, and P. Alken (2008), Estimating the day time Equatorial Ionization Anomaly strength from electric field, *J. Geophys. Res.,* **113,** A09310, doi:10.1029/2007JA012781.

Thayer, J. P., Killeen, T. L., McCormac, F. G., Tschan, C. R., Ponthieu, J.-J., and Spencer, N.W.: Thermospheric neutral wind signatures dependent on the east-west component of the interplanetary magnetic field for Northern and Southern Hemispheres, as measured from Dynamics Explorer-2, *Ann Geophys., 5,* 363–368, 1987.

Wang, H., H. Lühr and S.-Y. Ma, Solar zenith angle and merging electric field control of field-aligned currents: A statistical study of the southern hemisphere, *J. Geophys. Res.,* **110,** A03306, doi:10.1029/2004JA010530, 2005.

Watermann, J., P. Stauning, H. Lühr, P.T. Newell, F. Christiansen, and K. Schlegel, Are small-scale field-aligned currents and magnetosheath-like particle precipitation signatures of the same low-altitude cusp?, *Adv. Space Res., 43,* 41–46, 2009.
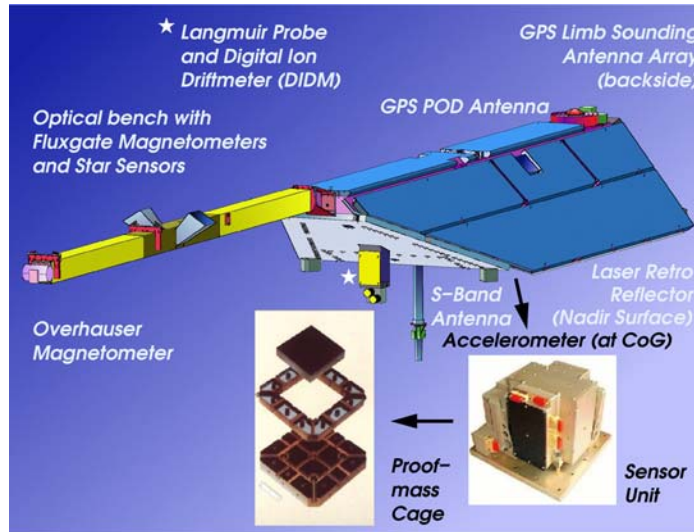
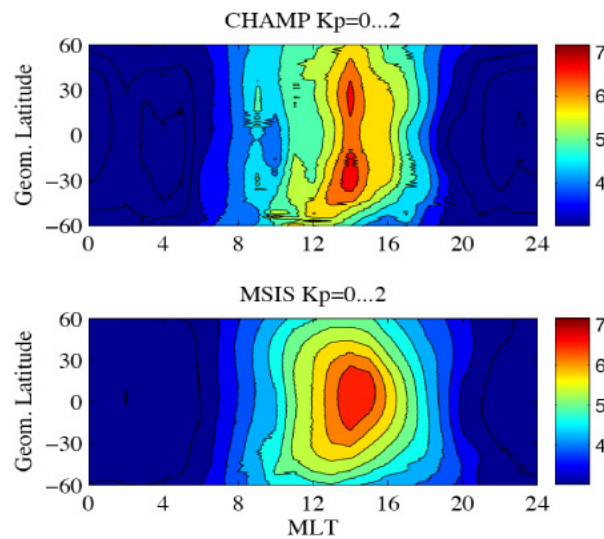**Fig. 1** Schematic illustration of the CHAMP satellite and the allocation of the scientific instruments.
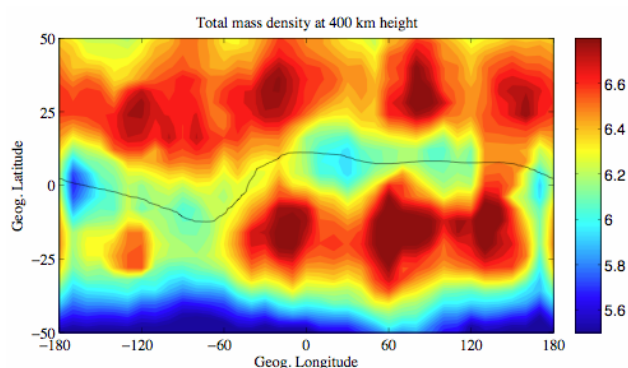

Fig. 2 Diurnal variation of the thermospheric mass density (in 10^{-12} kg/m^3). *(top)* Latitudinal distribution as observed by CHAMP; *(bottom)* as predicted by the MSIS model (after Fig. 2 of Liu et al., 2005).
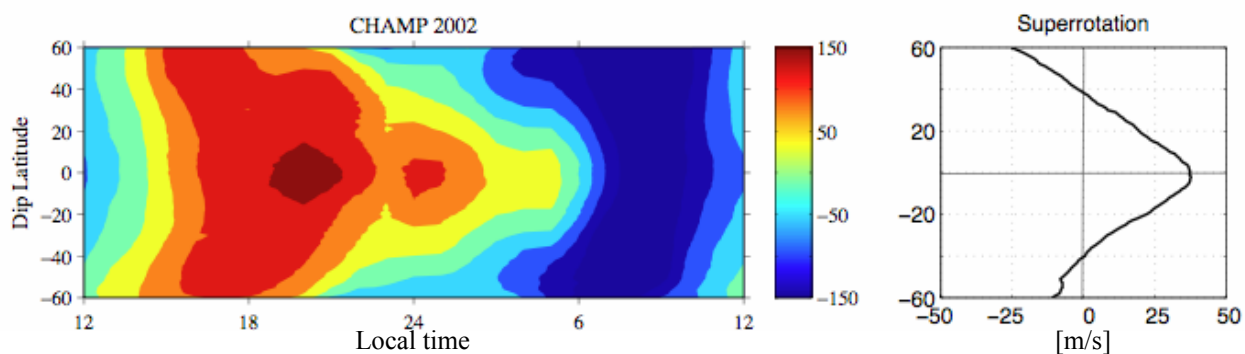
753
754
755
756
757
758

Fig. 3 Longitude/latitude distribution of the mass density (in 10^{-12} kg/m^3) on the dayside. The two bands of enhanced density are closely aligned to the magnetic dip-equator. (after Fig. 2 in Liu et al., 2007a).

759
760
761
762
763
764
765

Fig. 4 Diurnal variation of the thermospheric zonal wind (in m/s). *(left)* Latitudinal distribution as observed by CHAMP; (right) latitude variation of the longitudinally integrated zonal wind speed. (after Fig. 2 in Liu et al., 2009a).
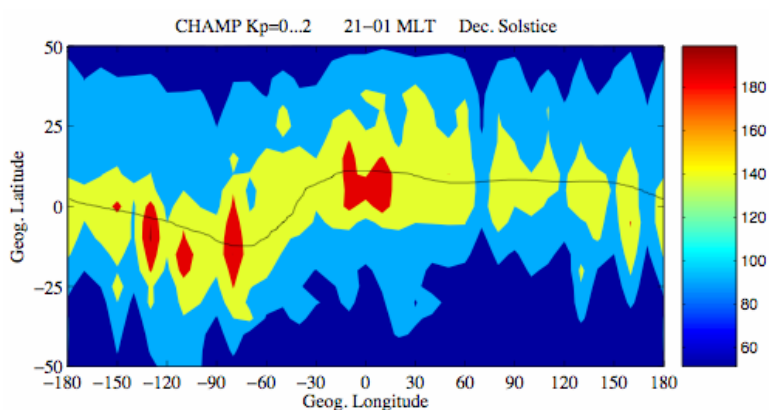
Fig. 5 Longitude/latitude distribution of the zonal wind (in m/s) on the night side. The channel of enhanced velocity follows the latitude variation of the magnetic dip-equator. (after Fig. 1 in Liu et al., 2009a).

771
772

CHAMP, 2003, June solstice, NH
12 MLT

CHAMP, 2003, June solstice, SH
12 MLT
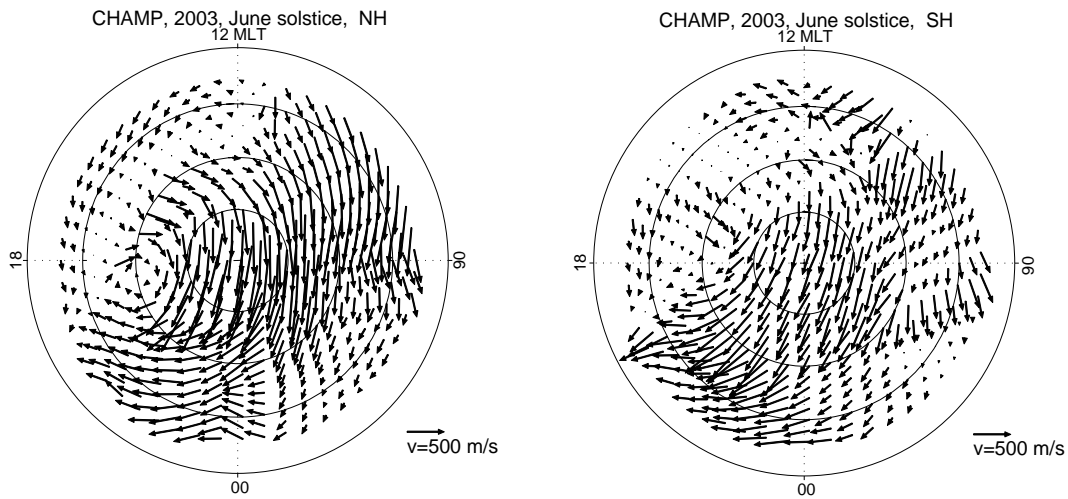
773
774 **Fig. 6** Distribution of mean thermospheric wind vectors in the Northern (summer) *(left)* and Southern
775 (winter) *(right)* hemispheres for June solstice 2003. **Concentric circles mark magnetic latitude at 10°**
776 **spacing (80°, 70°, 60° 50°).** (After Fig. 4 in Lühr et al., 2007)
777
778
779
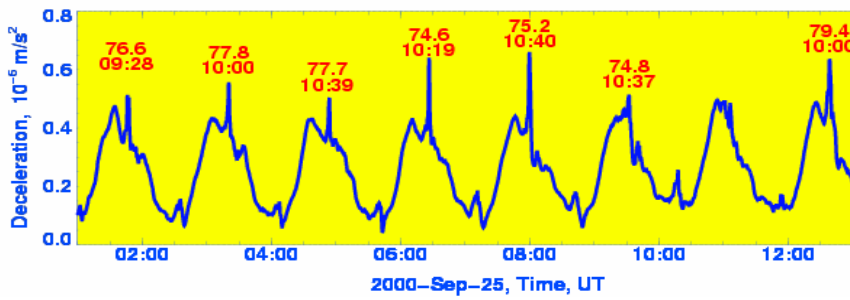
780
781
782 **Fig. 7** Deceleration of CHAMP by air drag. Local peaks in air drag are experienced in the cusp region. (after
783 Fig. 1 in Lühr et al., 2004).
784

785
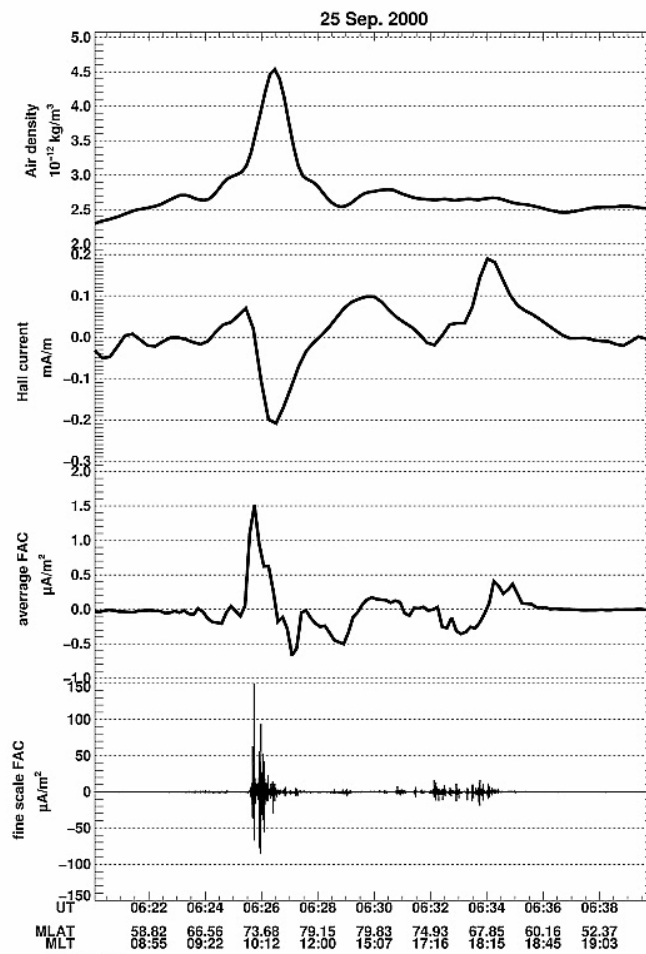
786
787
788 **Fig. 8** Synoptic view of the cusp-related density anomaly together with collocated ionospheric
789 currents. *(from top to bottom)* (1) mass density, (2) electrojet current density, (3) large-scale
790 field-aligned currents, and (4) kilometre-scale field-aligned currents.(After Fig. 2 in Lühr et al.,
791 2004).
792
793
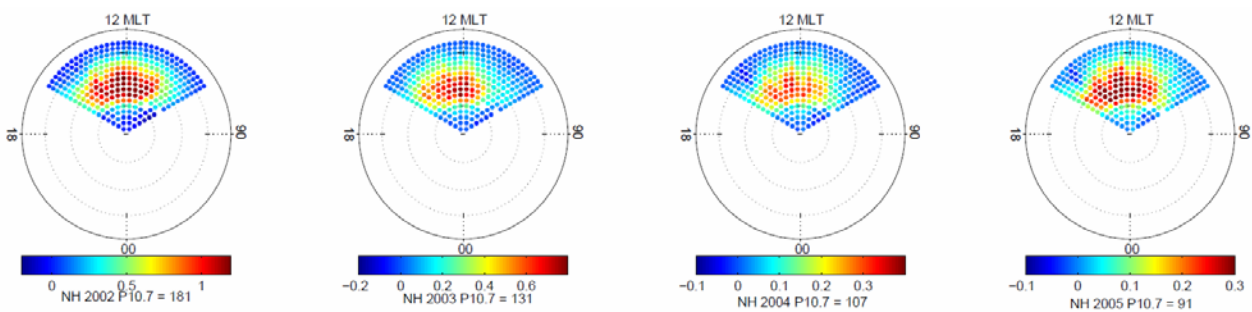
794
795
796 **Fig. 9** Average distribution of the cusp-related density anomaly amplitude (in 10^{-12} kg/m^3) in the
797 northern hemisphere for four successive years. Note the different density scales. Yearly averaged
798 solar flux values, P10.7, are listed below each plot. (After Fig. 4 in Rentz and Lühr, 2008).
799

19

800

801
802
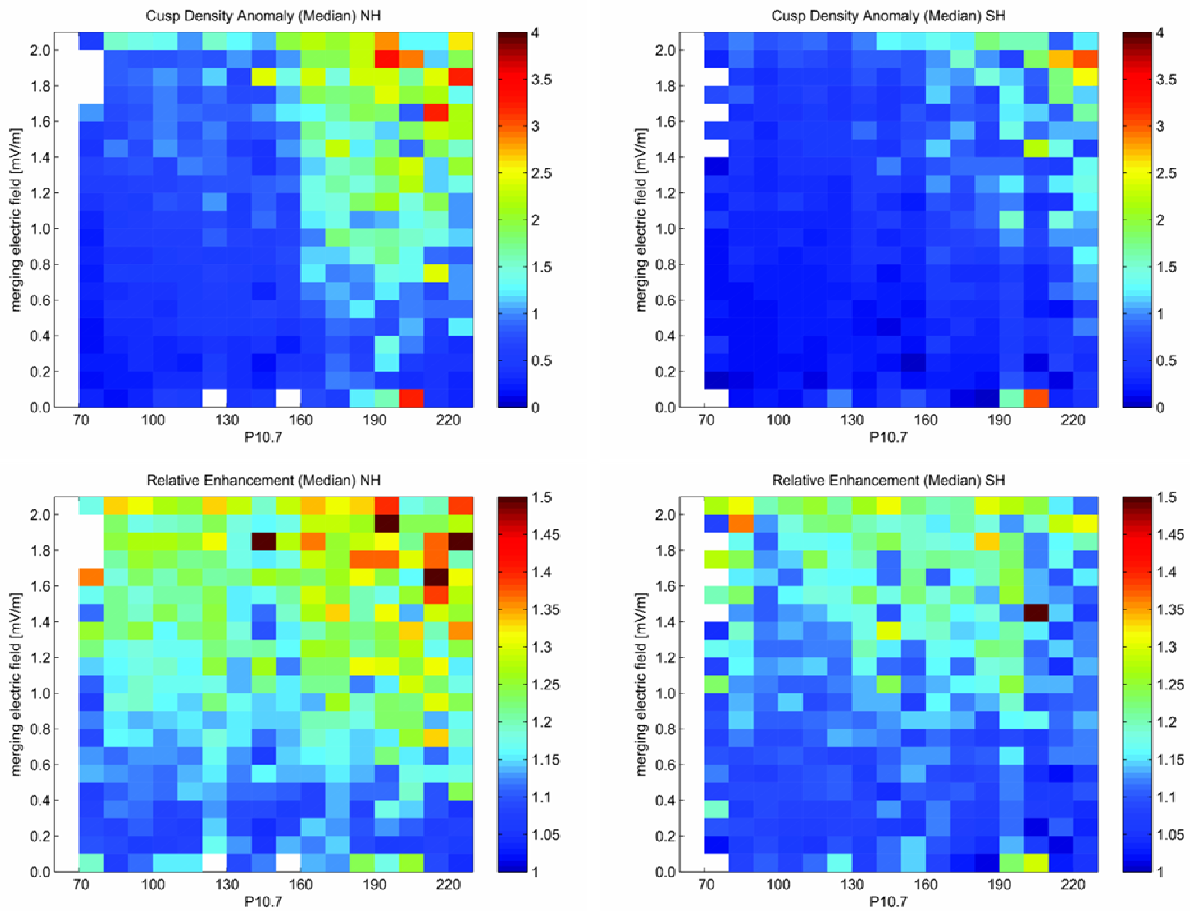
803 **Fig. 10** Dependence of the cusp-related density anomaly on solar flux level, P10.7 and on merging
804 electric field, separately for both hemispheres. *(top)* Amplitude of anomaly (in 10^{-12} kg/m^3),
805 *(bottom)* relative amplitude of anomaly with respect to background density.

806
807

808
809
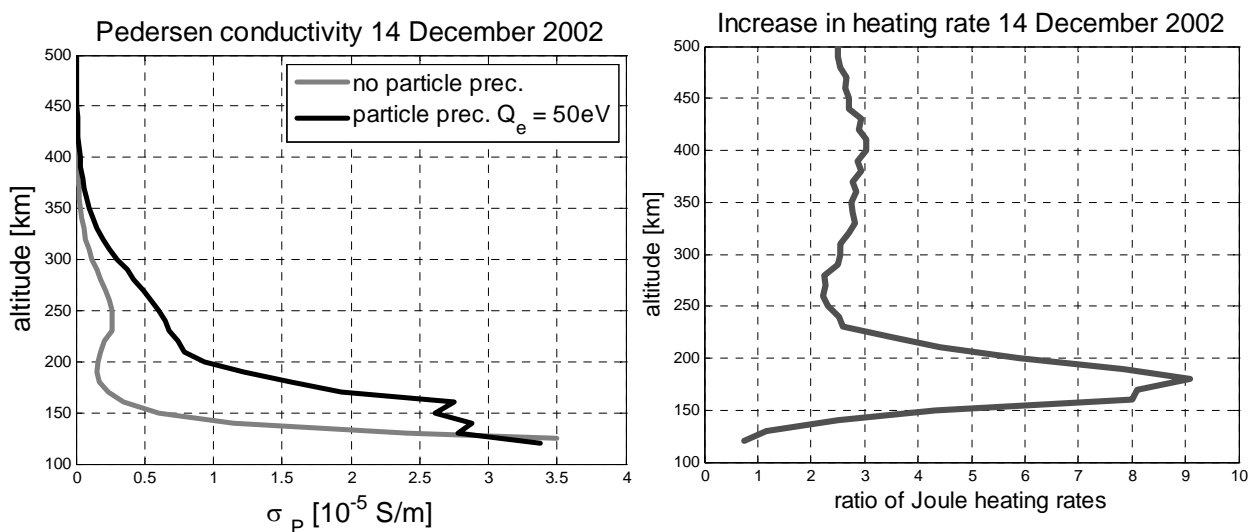
810 **Fig. 11** Effect of soft cusp-like particle precipitation on the conductivity and the Joule heating in the
811 ionosphere, as derived from the Sheffield High Latitude model. *(left)* Vertical profiles of the
812 Pedersen conductivity, *(right)* height profile of the relative Joule heating increase.

813
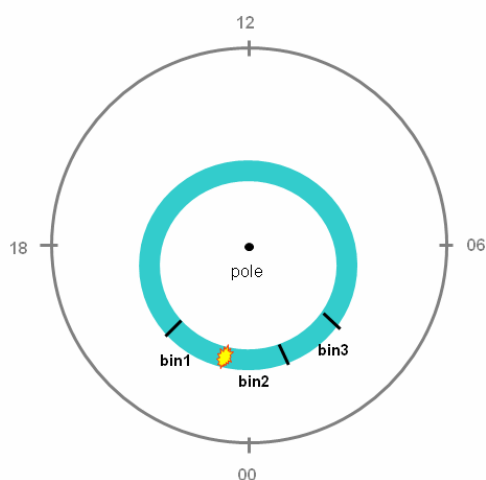
814
815
816 **Fig. 12** Scheme of binning CHAMP data by local time. Observations from passes to the west (0°-
817   30°) of the substorm onset are sorted into bin 1, passes to the east (0°-30° in long.) into bin 2,
818   and (30°-60° in long.) into bin 3.
819
820
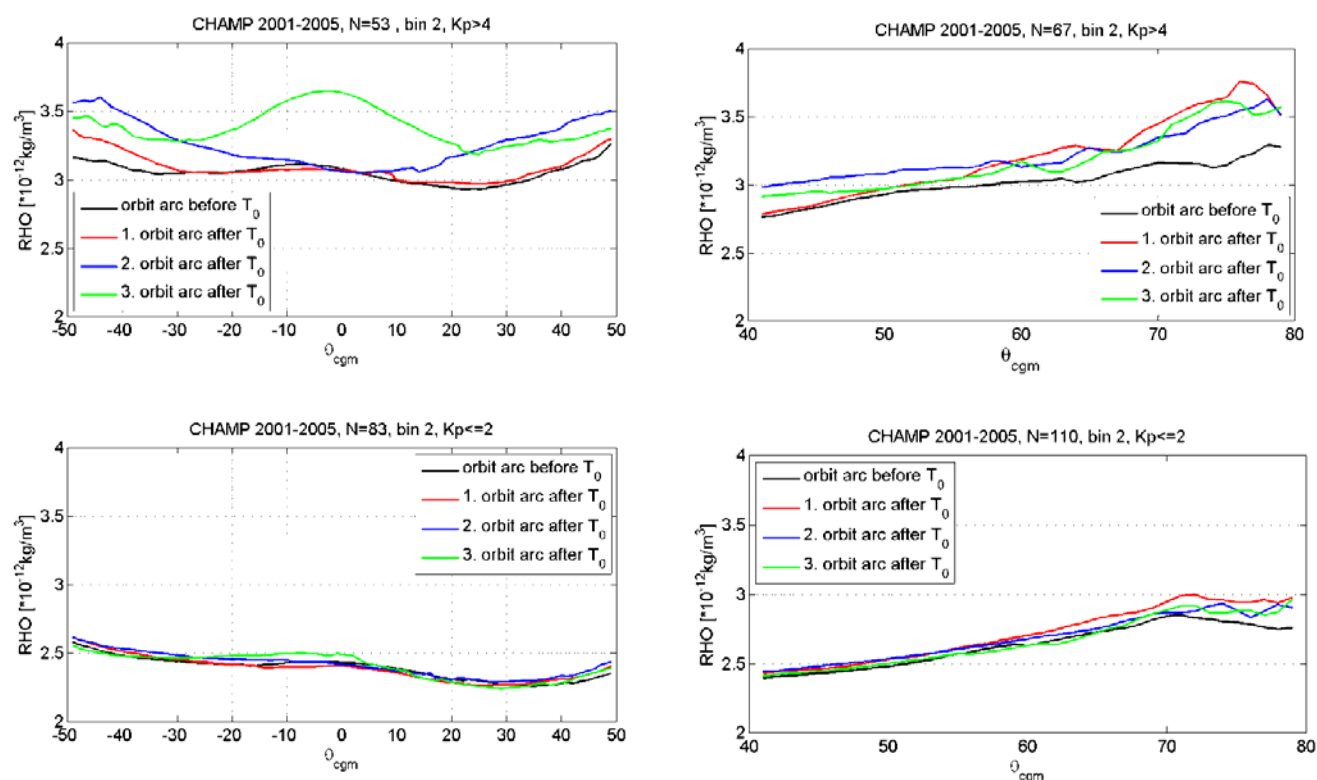
821
822
823 **Fig. 13** Latitude profiles of mean thermospheric density distribution before and after a substorm;
824   *(top row)* events from active period, *(bottom row)* events from quiet period, *(left frames)* low and
825   mid latitudes, *(right frame)* high latitudes. The colours of the curves mark different temporal
826   offsets to the substorm onset, T0. Black line: pass before T0; red line: 0.25–1.25 h after T0; blue
827   line: 1.75–2.75 h after T0; green line: 3.25–4.25 h after T0. (After Figs. 3 & 4 in Ritter et al.,
828   2010).
829

21

830
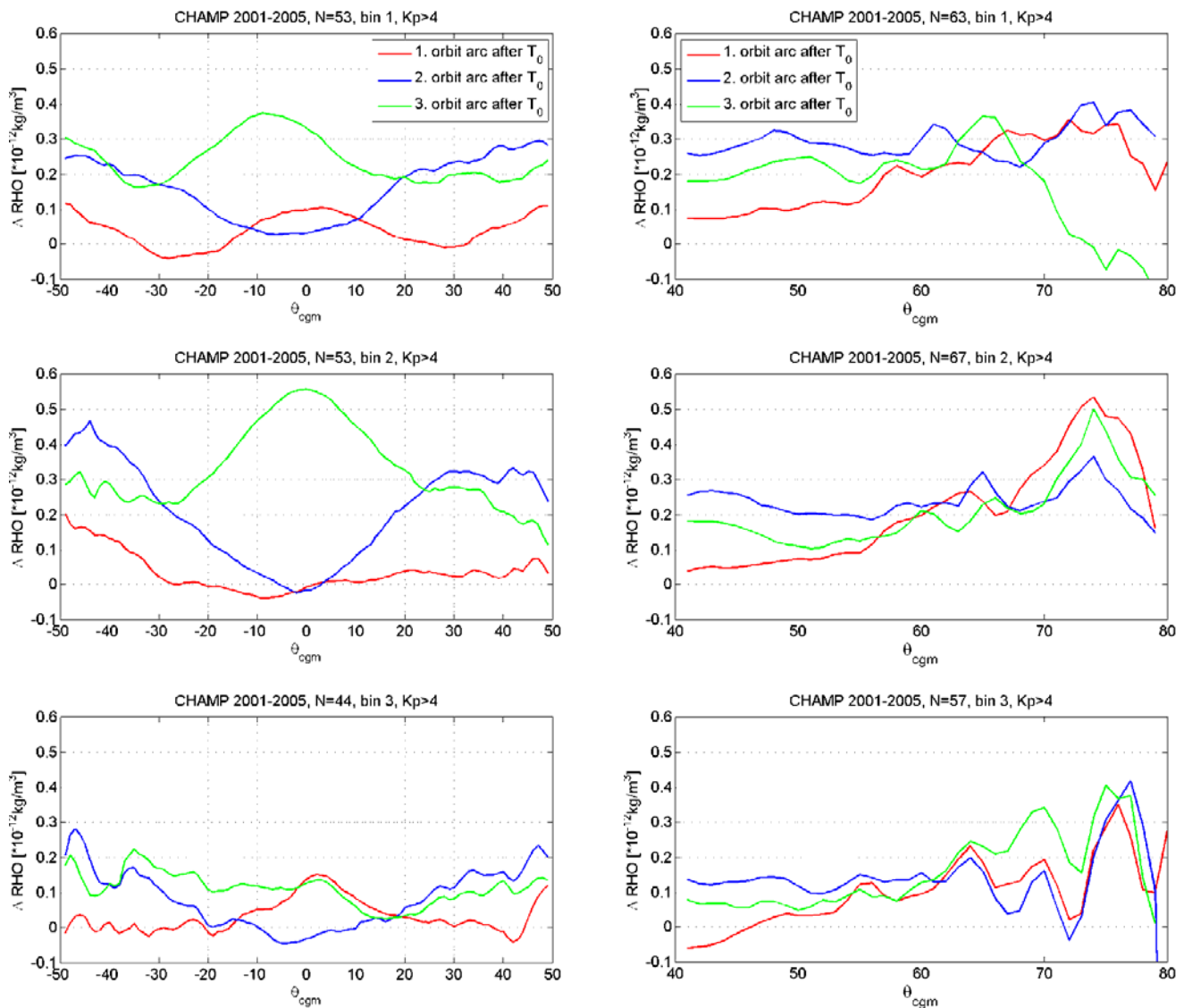
831
832
833 **Fig. 14** Temporal evolution of thermospheric density disturbance caused by a substorm during
834   magnetically active periods. Separate results for the three local time bins are shown. The
835   sequences of orbits and the colour-coded time offsets are the same as in Fig. 13. (After Fig. 5 in
836   Ritter et al., 2010).
837
838

839
840
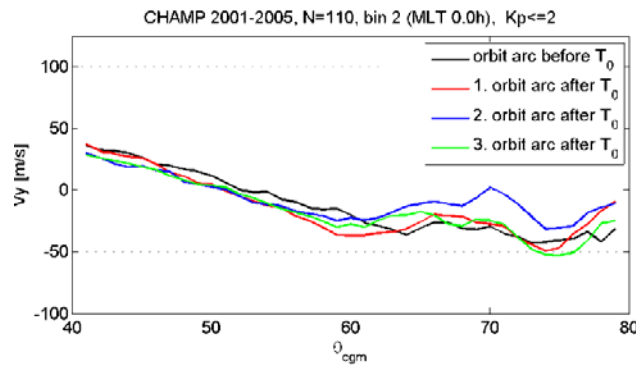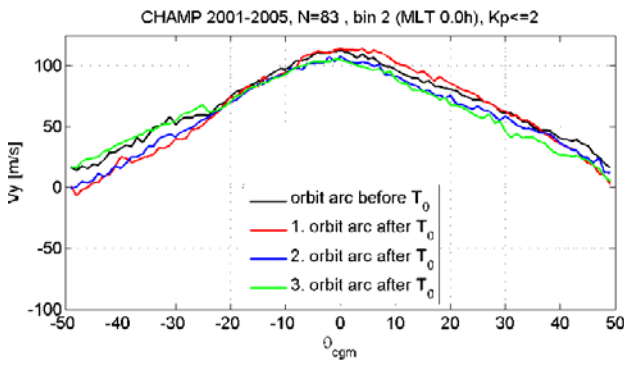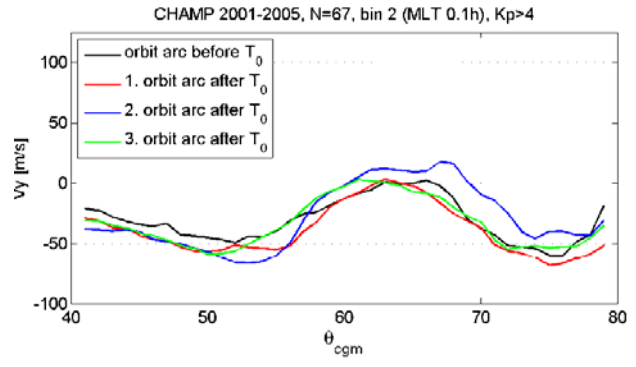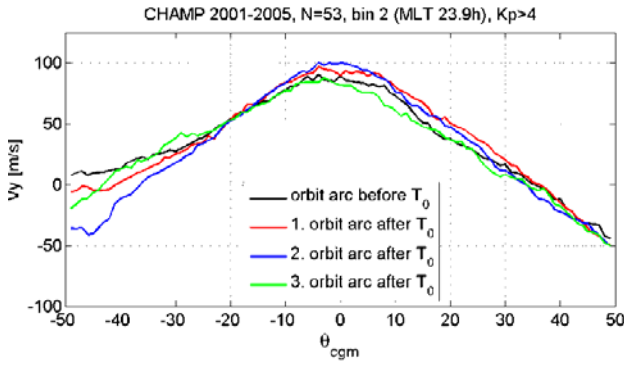
Fig. 15 Latitude profiles of the mean thermospheric zonal wind velocity around midnight; *(top row)* for high magnetic activity, *(bottom row)* for low activity. The colour-coding of the curves is the same as described in Fig. 13. (After Figs. 7 & 8 in Ritter et al., 2010).

844
845

846
847
848
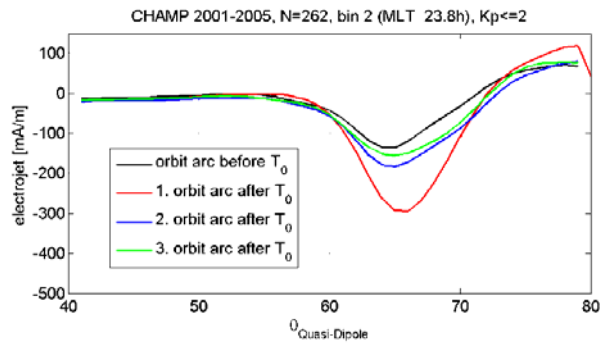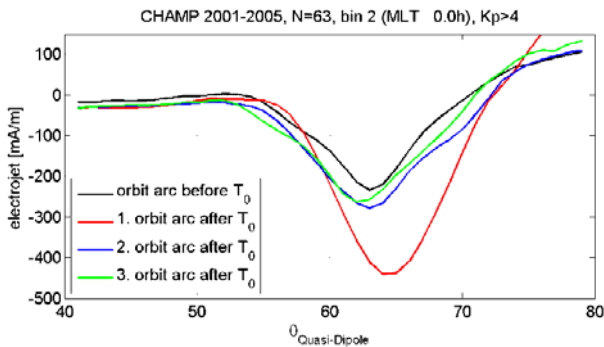
Fig. 16 Current density latitude profiles of the auroral electrojet in the midnight sector before and after a substorm; *(left frame)* high magnetic activity, *(right frame)* low activity. Negative values signify westward currents. The colour-coding of the curves is the same as described in Fig. 13.

852
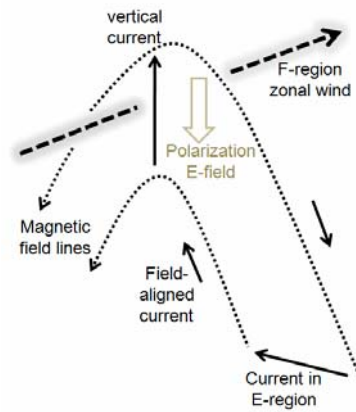
856 **Fig. 17** Schematic drawing of the F region dynamo concept. Shown is the configuration for
857   eastward zonal wind (evening time sector).

858
859
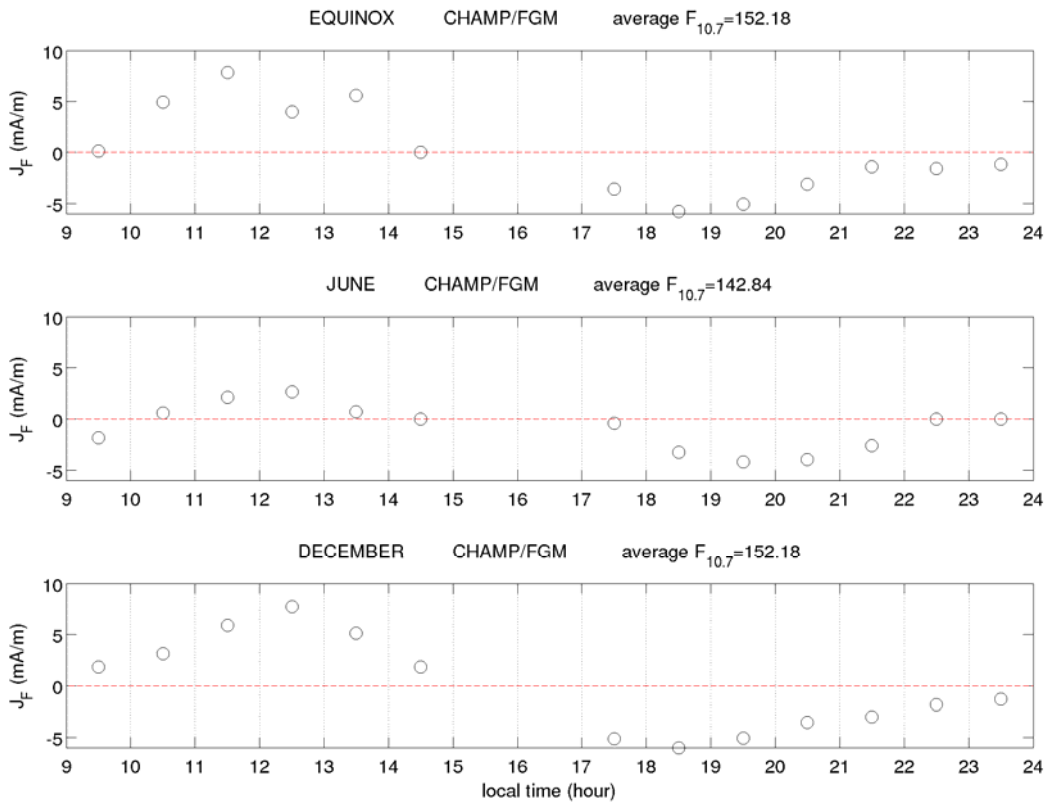
860
861 Fig. 18 Diurnal variation of the F region dynamo current zonal mean separately for the seasons.
862   Downward currents at the equator are denoted positive. Average solar flux levels (F10.7 index)
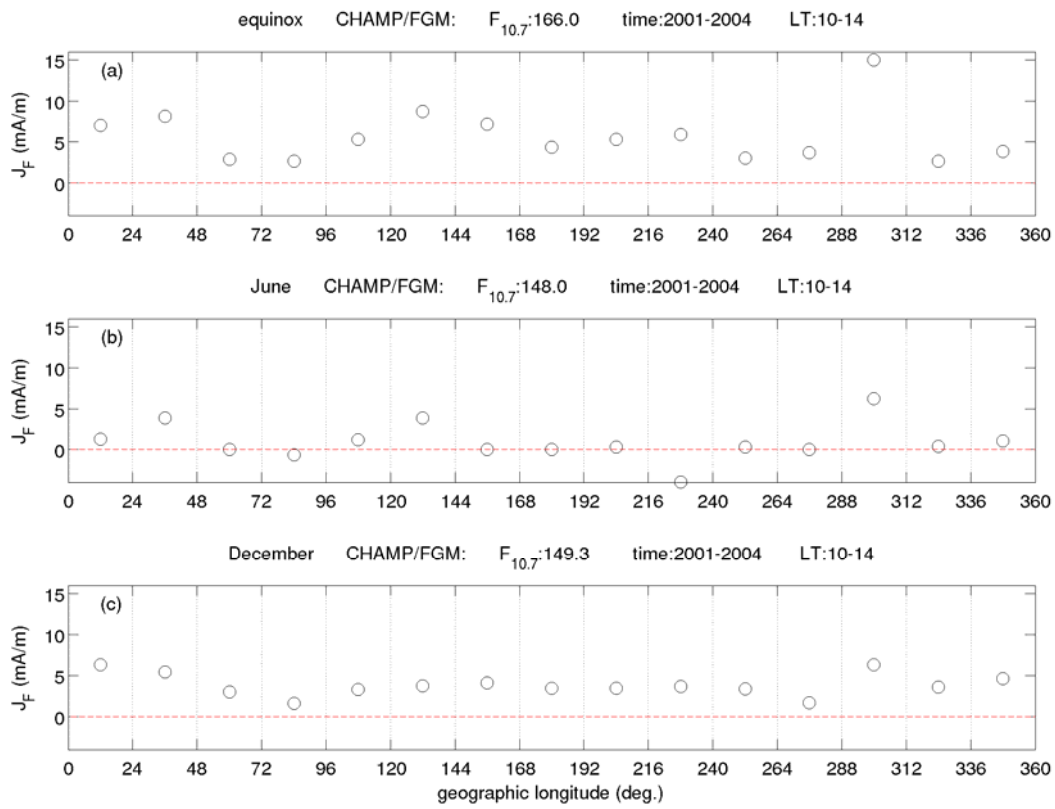863   for the seasons are given in the heading of each panel. (After Fig. 3 in Park et al., 2010a).
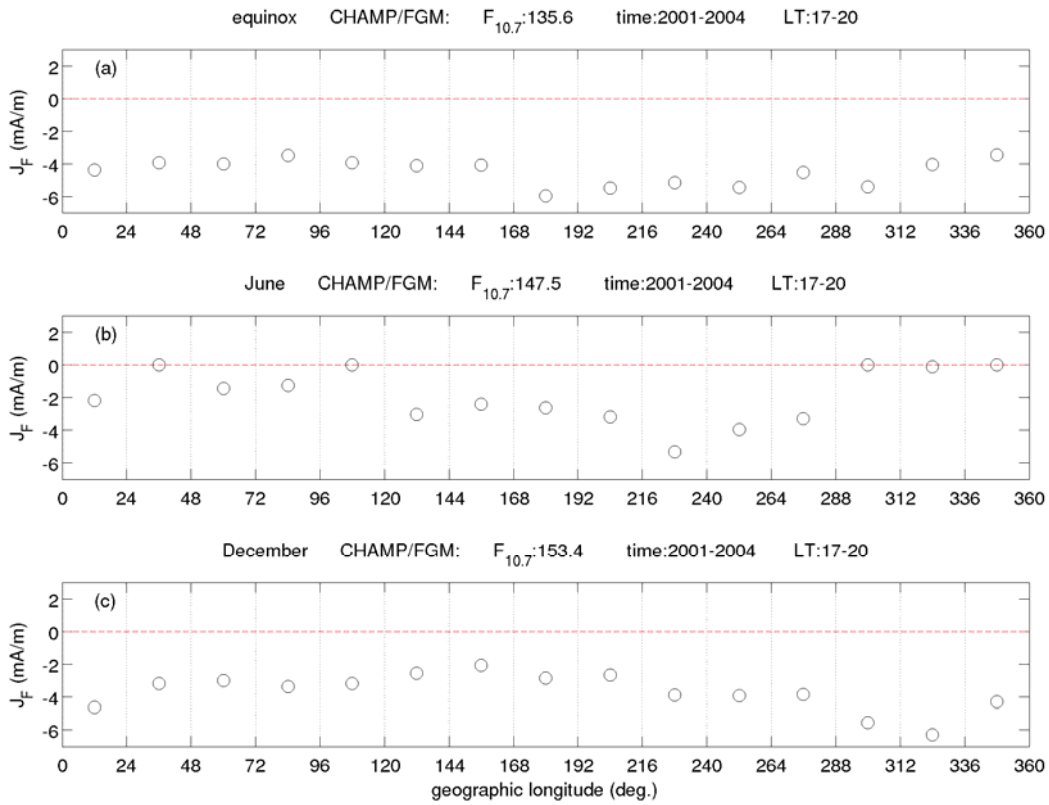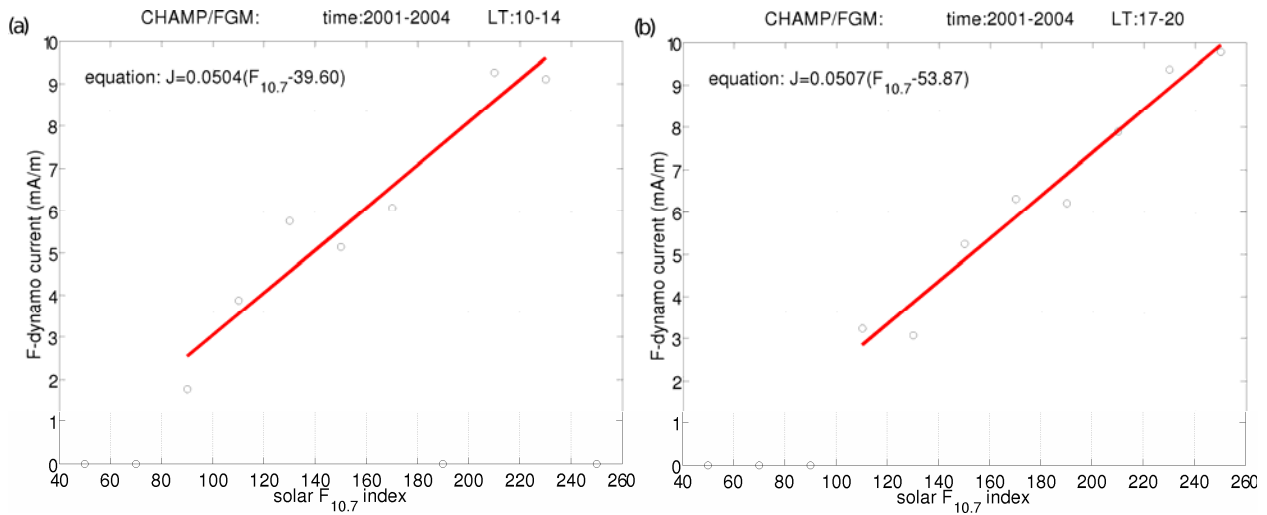864

865

Fig. 19 Longitude distribution of F region dynamo currents around the noon-time sector separatly
for each season, (a) equinoxes, (b) June solstice, and (c) December solstice.

Fig. 20 The same as Fig. 19, but for the evening sector.

Fig. 21 Dependence of F region dynamo current density on solar flux level (F10.7), separately for (a) noon sector and (b) dusk sector.